



A Low-mass Exoplanet Candidate Detected by *K2* Transiting the Praesepe M Dwarf JS 183

Joshua Pepper^{1,2}, Ed Gillen³, Hannu Parviainen⁴, Lynne A. Hillenbrand⁵, Ann Marie Cody⁶,
Suzanne Aigrain³, John Stauffer⁷, Frederick J. Vrba⁸, Trevor David^{5,12}, Jorge Lillo-Box⁹,
Keivan G. Stassun^{2,10}, Kyle E. Conroy², Benjamin J. S. Pope³, and David Barrado¹¹

¹Department of Physics, Lehigh University, 16 Memorial Drive East, Bethlehem, PA 18015, USA

²Department of Physics and Astronomy, Vanderbilt University, 6301 Stevenson Center, Nashville, TN 37235, USA

³Astrophysics Group, Cavendish Laboratory, J. J. Thomson Avenue, Cambridge CB3 0HE, UK

⁴Oxford Astrophysics, University of Oxford, Denys Wilkinson Building, Keble Road, Oxford OX1 3RH, UK

⁵Department of Astronomy, California Institute of Technology, 1200 E. California Boulevard, MC 249-17, Pasadena, CA 91125, USA

⁶NASA Ames Research Center, Mountain View, CA 94035, USA

⁷Spitzer Science Center, California Institute of Technology, Pasadena, CA 91125, USA

⁸U.S. Naval Observatory, Flagstaff Station, 10391 W. Naval Observatory Road, Flagstaff, AZ 86005-8521, USA

⁹European Southern Observatory (ESO), Alonso de Córdova 3107, Vitacura, Casilla 19001, Santiago de Chile, Chile

¹⁰Department of Physics, Fisk University, Nashville, TN 37208, USA

¹¹Depto. de Astrofísica, Centro de Astrobiología (CSIC-INTA), ESAC campus E-28691 Villanueva de la Cañada (Madrid), Spain

Received 2016 July 8; revised 2017 February 2; accepted 2017 February 5; published 2017 March 24

Abstract

We report the discovery of a repeating photometric signal from a low-mass member of the Praesepe open cluster that we interpret as a Neptune-sized transiting planet. The star is JS 183 (HSJ 163, EPIC 211916756), with $T_{\text{eff}} = 3325 \pm 100$ K, $M_* = 0.44 \pm 0.04 M_{\odot}$, $R_* = 0.44 \pm 0.03 R_{\odot}$, and $\log g_* = 4.82 \pm 0.06$. The planet has an orbital period of 10.134588 days and a radius of $R_p = 0.32 \pm 0.02 R_J$. Since the star is faint at $V = 16.5$ and $J = 13.3$, we are unable to obtain a measured radial velocity orbit, but we can constrain the companion mass to below about $1.7 M_J$, and thus well below the planetary boundary. JS 183b (since designated as K2-95b) is the second transiting planet found with *K2* that resides in a several-hundred-megayear open cluster; both planets orbit mid-M dwarf stars and are approximately Neptune sized. With a well-determined stellar density from the planetary transit, and with an independently known metallicity from its cluster membership, JS 183 provides a particularly valuable test of stellar models at the fully convective boundary. We find that JS 183 is the lowest-density transit host known at the fully convective boundary, and that its very low density is consistent with current models of stars just above the fully convective boundary but in tension with the models just below the fully convective boundary.

Key words: galaxies: star clusters: individual (Praesepe) – planets and satellites: detection

1. Introduction and Context

Open clusters have been one of the preferred locations for exoplanet searches since the early days of exoplanet discovery. Representing relatively compact, coeval populations of stars with similar composition, they serve as desirable test beds for comparing planet frequencies and properties across various stellar parameters. They have been especially selected for transit searches, since many open clusters are compact on the sky, requiring few separate telescope pointings.

Early transit searches for planets in clusters failed to detect planets (e.g., Mochejska et al. 2005, 2006, 2008; von Braun et al. 2005; Burke et al. 2006; Aigrain et al. 2007; Pepper et al. 2008; Hartman et al. 2009). It appears that the primary reason for this is that such searches were sensitive only to hot Jupiters, which are intrinsically rare (Gould et al. 2006; Wright et al. 2012), and that most open clusters do not have enough members for high-probability detection of even one hot Jupiter (Pepper & Gaudi 2005; Aigrain & Pont 2007; Beatty & Gaudi 2008; van Saders & Gaudi 2011). Radial velocity (RV) searches suffer less from the low probability of fortuitous orbital inclination angles required for transit searches. Via an RV survey, Quinn et al. (2012) discovered two Jupiter-mass planets in the open cluster Praesepe, with Malavolta et al. (2016) finding an additional much higher mass planet in one of

these two systems, and Quinn et al. (2014) reported a Jupiter-mass planet in the Hyades cluster. Three additional Jupiter-mass RV planets were reported in M67 by Brucalassi et al. (2014). Planets have also been found orbiting evolved members of open clusters (Lovis & Mayor 2007; Sato et al. 2007).

The higher frequency of smaller planets compared to hot Jupiters (Howard et al. 2012; Petigura et al. 2013) presents an opportunity to revisit open clusters as transit search targets. Missions like *Kepler* (Borucki et al. 2010) have the photometric precision to detect small planets, and the repurposed *Kepler* mission *K2* (Howell et al. 2014) covers a much larger fraction of the sky, allowing for multiple open clusters to be observed. The first transiting planets orbiting stars in clusters were claimed by Meibom et al. (2013), who reported that two members of the ~ 1 Gyr open cluster NGC 6811 in the *Kepler* field host sub-Neptune-sized planet candidates associated with G-type main-sequence stars. From *K2* mission data, both Mann et al. (2016b) and David et al. (2016a) reported the independent discovery of the Neptune-sized planet known as K2-25b orbiting the ~ 600 – 800 Myr old Hyades cluster member Han87, with a late M spectral type.

There are benefits to detecting planets in young (sub-Gyr) clusters. At early ages, the dynamical environments of the planetary systems might not be settled down. Planet–planet interactions might still be occurring at that stage. Once a statistically significant sample of extrasolar planets is found in

¹² NSF Graduate Research Fellow.

clusters with various ages, we can explore the evolution of planetary systems at early times, with implications for planetary migration and dynamical stability. That process might also provide insight into the actual locations in the disk where the planets originally formed.

M dwarfs are of specific interest as transiting planet hosts, given the larger transit signal afforded by smaller stars. Also, it appears that M dwarfs are more likely than earlier-type stars to host planets (Dressing & Charbonneau 2013), with implications for the frequency of planets in the habitable zones of M dwarfs (Dressing & Charbonneau 2015). According to the NASA Exoplanet Archive,¹³ there are only 25 known M dwarfs ($T_{\text{eff}} \leq 3850$ K) with confirmed transiting planets. Since M dwarf properties are notoriously difficult to pin down (e.g., activity can inflate them, empirical relations for M dwarf radii suggest metallicity dependence, etc.; Stassun et al. 2012; Mann et al. 2016a), this limits the precision on the transiting planet radii. Indeed, of the 25 previously known M dwarfs with transiting planets, only two (GJ 1132, GJ 1214) have measured parallaxes permitting a direct determination of the stellar radius and a spectroscopically determined metallicity to permit the most reliable stellar mass estimates from empirical relations, and because they are field stars, it is not possible to determine robust stellar ages. The expected arrival of parallaxes from the upcoming *Gaia* second data release promises to provide precise stellar and planetary parameters for many more transiting systems (see, e.g., Stassun et al. 2016).

In this paper we report the discovery of a Neptune-sized planet transiting an M dwarf member of the Praesepe open cluster, observed by the *K2* mission. The star is alternately referred to as JS 183 (Jones & Stauffer 1991), HSHJ 163 (Hambly et al. 1995), 2MASS J08372705+1858360 (Cutri et al. 2003; Skrutskie et al. 2006), and EPIC 211916756 (Huber et al. 2015). In the course of this work, this star was examined by other researchers and given the official *K2* name K2-95b; however, since this star has been known as JS 183 in the literature for some time, we use the name JS 183 in this paper. Since the host star is a member of a well-studied stellar population with known distance, metallicity, and age, it is possible to obtain precise stellar and therefore planet properties and to assign a precise age to the system. Section 2 discusses the properties of the host star. Section 3 presents the archival and newly obtained photometric, spectroscopic, and imaging data that we use in this analysis. Section 4 presents the main results of this study, including a precise transit model, a detailed spectral energy distribution (SED) analysis providing precise stellar properties, an analysis of RV observations placing an upper limit on the planet mass, and the final adopted planet properties, showing the planet to be a Neptune-sized planetary mass object transiting an M3.5-type cluster star. We summarize our findings and conclusions in Section 6.

2. Praesepe Membership and Stellar Properties from the Literature

JS 183 is a modestly active M dwarf (spectral type \approx M3.5e; Adams et al. 2002), high-probability member of the Praesepe cluster. In this section we briefly summarize the evidence for cluster membership and chromospheric activity, as well as salient general properties of the Praesepe cluster that therefore apply to JS 183. Table 1 summarizes the basic properties of

Table 1
Basic Properties of JS 183

Property	Value	References
Names	JS 183, HSHJ 163, 2MASS J08372705 +1858360, EPIC 211916756	1, 2, 3, 4
R.A. (J2000.0)	08:37:27.06	3
Decl. (J2000.0)	+18:58:36.07	3
Spectral type	M3.5e	5
[Fe/H]	0.1–0.27	6
V mag	17.08	7

References. (1) Jones & Stauffer 1991; (2) Hambly et al. 1995; (3) Cutri et al. 2003; Skrutskie et al. 2006; (4) Huber et al. 2015; (5) Adams et al. 2002; (6) Pace et al. 2008; (7) L. M. Rebull et al. (2016, in preparation).

JS 183, including a digest of the various identifiers with which it has appeared in the literature. The *K2* name is EPIC 211916756.

2.1. Cluster Membership

A number of focused studies and all-sky surveys have determined cluster membership probabilities for JS 183 based on proper motion and/or RVs. Kraus & Hillenbrand (2007) included JS 183 in their focused proper-motion study of the Praesepe cluster, finding a membership probability of 99.4%. Boudreault et al. (2012) similarly combined UKIDSS proper motions and photometry to obtain a cluster membership probability of 92%.

JS 183 has also been included in all-sky proper-motion surveys, with the following proper motions ($\mu_{\alpha}, \mu_{\delta}$) [mas yr⁻¹] from USNO B1, PPMX, and URAT, respectively: (−34, −14), (−39, −17), (−34, −17). These agree well with the mean Praesepe cluster motion, which has been reported as (−29, −7), (−34, −7.5), and (−36, −13) from Adams et al. (2002), Boudreault et al. (2012), and Kraus & Hillenbrand (2007), respectively. In summary, there is strong consensus in the literature that JS 183 is a high-probability member of the Praesepe cluster based on its proper motion and photometry.

2.2. Cluster Age and Metallicity

The accepted age of the Praesepe cluster is \approx 600 Myr (e.g., Adams et al. 2002), although an older age of \approx 800 Myr was recently advocated (Brandt & Huang 2015). Praesepe has been found to have a supersolar metallicity, with most values around [Fe/H] \approx 0.1 (for a good summary see Boesgaard et al. 2013), but with some values as high as [Fe/H] = 0.27 ± 0.10 (e.g., Pace et al. 2008). In our analysis we make use of the metallicity to estimate the stellar radius expected from empirical M dwarf radius relations, and we use the cluster age to place the JS 183 planet system in the context of other systems of known age.

2.3. Stellar Activity

Barrado y Navascués et al. (1998) conducted a comparison of Praesepe and Hyades chromospheric/coronal activity. Their reported data for JS 183 (identified as HSHJ 163) from a 1997 December Keck/HIRES observation indicated a Balmer line equivalent width $\text{EW}(\text{H}\alpha) = 0.00 \text{ \AA}$ and X-ray luminosity $\log L_X < 28.07 \text{ erg s}^{-1}$. Adams et al. (2002) used low-resolution spectroscopy to obtain a spectral type of M3.5e, indicating activity, with $\text{EW}(\text{H}\alpha) = -0.3 \text{ \AA}$. Kafka & Honeycutt (2006)

¹³ <http://exoplanetarchive.ipac.caltech.edu/index.html>

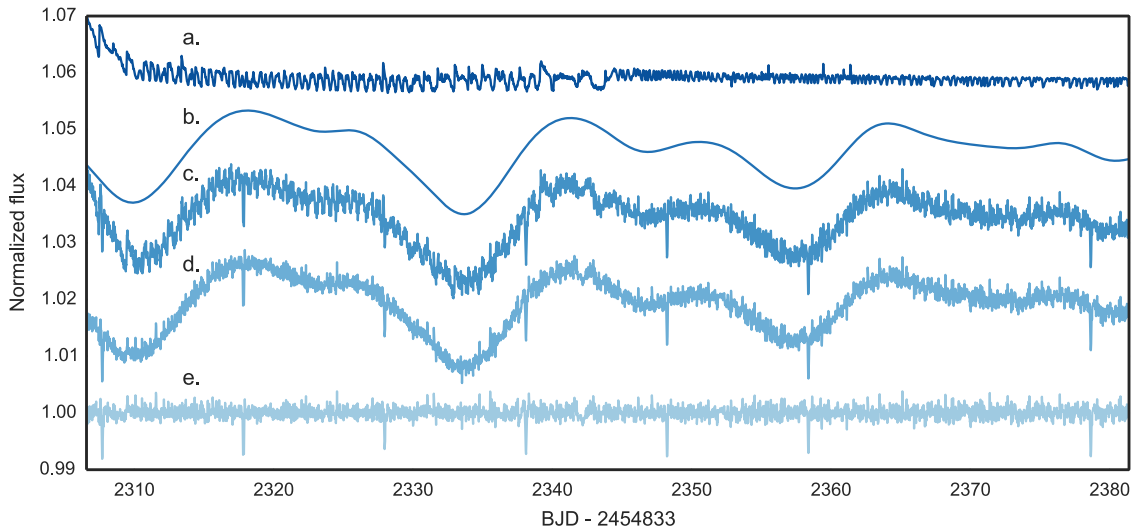


Figure 1. *K2* light curve of JS 183. From the top are the K2SC models of the pointing systematics (a) and of the stellar variability (b). Then the original PDC light curve (c), the systematics-corrected version (d), and the fully detrended version—after removal of the stellar variability model (e). Version (d) was used in the transit search and modeling described in Section 4.1.1, while version (e) was used in the modeling described in Section 4.1.2. Note that there was a short gap in the original data at the time of the penultimate transit, which is why it appears to be missing.

also report an $\text{EW}(\text{H}\alpha) = -0.16 \text{ \AA}$. In summary, all of these studies show $\text{H}\alpha$ just very weakly in emission or filled in, suggesting modest chromospheric activity.

3. New Observations and Analysis

3.1. *K2* Observations and Light Curve Properties

The photometric observations from *K2* require considerable attention to the construction of proper apertures and removal of systematic noise (see, e.g., Vanderburg & Johnson 2014; Foreman-Mackey et al. 2015; Aigrain et al. 2016). Here we describe the extraction of the light curve of JS 183, the removal of systematics, the identification of the transit signal, and the characterization of out-of-transit variability.

3.1.1. Light Curve Preparation

JS 183 was observed by *K2* in its Campaign 5 field, from MJD 57,139.13 to 57,213.93, acquiring 3448 photometric observations at the standard 30-minute cadence. We downloaded the light curve file for JS 183 from the Mikulski Archive for Space Telescopes (MAST), which includes both Simple Aperture Photometry (SAP) fluxes and a version of the light curve after application of the *Kepler* Pre-search Data Conditioning (PDC) pipeline (Twicken et al. 2010; Smith et al. 2012; Stumpe et al. 2012). This algorithm effectively models trends that are common to the ensemble of light curves, which was sufficient for the nominal *Kepler* mission but does not account for the diversity of pointing-related systematics present in *K2* (see Vanderburg & Johnson 2014; Van Cleve et al. 2016, for details). We therefore additionally used the K2SC Gaussian process (GP) based systematics correction algorithm of Aigrain et al. (2016) to detrend both SAP and PDC light curves with respect to pointing variations. This algorithm models the stellar variability simultaneously with the pointing-dependent systematics and outputs a model for each component, so that either or both can be subtracted at will.

While the PDC light curve is usually the version of choice to look for transit signals, the PDC pipeline sometimes removes true astrophysical signals on timescales >20 days. Therefore, it is

usually considered advisable to use the SAP light curve as a starting point for any detailed analysis of the transits and out-of-transit variability. However, after a visual comparison of the SAP and PDC light curves (both before and after modeling with K2SC), we opted to work with the PDC light curve throughout this paper. This decision was made because the SAP light curve is affected by long-term trends that are probably systematic, and because the K2SC modeling of the (shorter-timescale) pointing-related systematics is less successful in the SAP than in the PDC light curve for this particular object. Figure 1 shows the *K2* PDC light curve for JS 183 along with the variability and systematics models from K2SC, as well as the light curve after correcting systematics only, and after also removing the variability model. Figure 2 shows the individual transits in more detail, using the detrended version of the light curve shown as version (e) in Figure 1. We estimated the 6 hr Combined Differential Photometric Precision (CDPP) of the fully detrended light curve as 274 ppm (the CDPP is the standard measure of photometric precision on transit timescales for *Kepler* light curves; see Christiansen et al. 2012).

3.1.2. Transit Detection

The transits of JS 183 were identified independently by two methods. The first was visual inspection of the SAP and PDC light curves for all likely members of Praesepe observed by *K2* (the transits are clearly visible in Figure 1). The second was a systematic search for transits, which we performed for all the K2SC-detrended PDC light curves for Campaign 5 (after subtraction of both systematics and variability models), in which JS 183 was identified. The details of this search are given in Pope et al. (2016), who also report the full list of transit candidates. The initial search found transits with a period of ~ 10.1 days, a depth of ~ 7 parts per thousand, and a duration of ~ 3 hr, consistent with a transiting companion somewhat smaller than Jupiter. A full analysis of the transits is presented in Section 4.1.

3.1.3. Out-of-transit Variability and Rotation

The light curve displays smooth, quasi-periodic variations with a peak-to-peak amplitude of $\sim 2\%$, which we attribute to

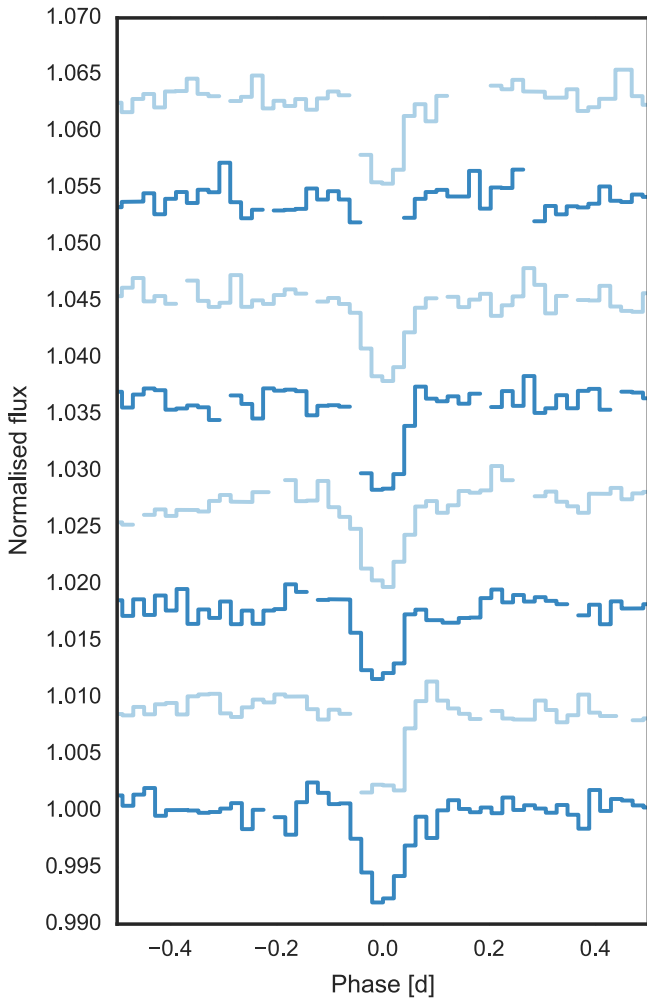


Figure 2. Individual transits in the K2SC-detrended PDC light curve of JS 183. The transits are shown in chronological order from bottom to top, with a vertical offset applied for clarity.

rotational modulation due to starspots. The K2SC pipeline detected these variations and automatically switched to using a quasi-periodic GP covariance function to model them. This covariance function is parameterized by a period, an amplitude, a periodic length scale (which controls the number of inflexions per period), and an evolutionary timescale. The best-fit values of the period and evolutionary timescale parameters were 25.5 and ~ 200 days, respectively. The former can be interpreted as an estimate of the host star’s rotation period, while the latter suggests that the characteristic lifetime of the active regions present on the star’s surface at the time of the observations was roughly 8 times the rotation period. Recent studies of rotation in Praesepe (Agueros et al. 2011; Delorme et al. 2011; Douglas et al. 2014) show a tight relationship between period and color from $J - K \sim 0.25$ to $J - K \sim 0.8$, with periods tightly clustered around values ranging from ~ 6 days at the bluer end to ~ 10 days at the redder end. Redward of $J - K \sim 0.8$, however, the rotation period distribution becomes extremely broad, with periods ranging from 0.2 to >30 days irrespective of color. With $J - K = 0.84$, JS 183 lies in this second regime, and a rotation period of ~ 25 days is thus consistent with, albeit at the longer end of, the expected range.

3.2. Follow-up Light Curve Observations

In order to confirm the properties of the transit, we observed JS 183 on the night of UT 2016 February 26, using a thinned, back-side-illuminated Tektronix 2048 CCD (“new2K”) on the USNO, Flagstaff Station 40-inch telescope. A standard Kron–Cousins I -band filter was used with an exposure time of 120 s (based on test exposures from the previous night) and readout overhead of 51 s, resulting in a net observing cadence of 171 s. A total of 160 frames of JS 183 were obtained between UT 02:17 and UT 09:51. The frames were processed in real time with bias and flat-field frames obtained at the beginning of the night. Sky conditions were clear, although the seeing gradually worsened from about $1''.2$ FWHM at the beginning of the night to about $2''.2$ at the end of the exposure series.

As a result of these observations, we obtain a clear detection of the transit, albeit at a lower photometric precision than from $K2$. The detection took place about 221 days after the last of the $K2$ observations, an offset of 22 orbital periods. The USNO light curve is shown in conjunction with the $K2$ light curve in Figure 3. In Section 4.1 we show that incorporating the USNO light curve into the analysis gives a consistent solution with modeling the $K2$ light curve alone.

3.3. Spectroscopic Observations and Radial Velocities

We observed JS 183 with the Keck/HIRES spectrograph (Vogt et al. 1994) at six epochs: one in 1997 as part of another program, two in 2015, and three in 2016 as follow-up to the $K2$ light curve (see Table 2). All observations achieved spectral resolution $R > 48,000$. The 1997 observation used a wavelength range of 6300–8725 Å, while the 2015 and 2016 observations used a range of 4800–9200 Å, except for the final one. The images were processed and spectra extracted and calibrated using the MAKEE software¹⁴ written by Tom Barlow. The spectral type estimate for the star from these high-dispersion data is M3–M4. We infer the presence of a small amount of stellar chromospheric activity based on the fact that the $H\alpha$ line is completely filled in, with no apparent absorption or emission, and thus no equivalent width measurement is possible. The $H\beta$ line is weakly in emission with $EW(H\beta) = -0.45$ Å.

From these spectra we obtained single-lined RVs of the host star. Heliocentric velocities were measured in the four Keck/HIRES spectra by cross-correlating with RV standards obtained at the same time as the program spectra. The mean and standard deviations of the multiorder RVs are summarized in Table 2. The systemic RV inferred from our four measurements is 35.34 ± 0.17 km s⁻¹.

The mean RV of the Praesepe cluster based on high-resolution spectra of FGK members has been determined as 37.7 km s⁻¹ (Barrado y Navascués et al. 1998) and as 34.6 ± 0.7 km s⁻¹ (Mermilliod & Mayor 1999). The mean RV of JS 183 from the observations reported here is in between these values; thus, we conclude that JS 183 is dynamically consistent with Praesepe cluster membership.

In addition, Barrado y Navascués et al. (1998) obtained medium-resolution spectra of a number of M dwarfs in Praesepe, including JS 183 (using the designation HSHJ 163). For JS 183, Barrado y Navascués et al. (1998) measure an RV of 32.4 km s⁻¹, which was consistent with Praesepe membership given the low RV accuracy from that paper, which was

¹⁴ <http://www.astro.caltech.edu/~tb/makee/>

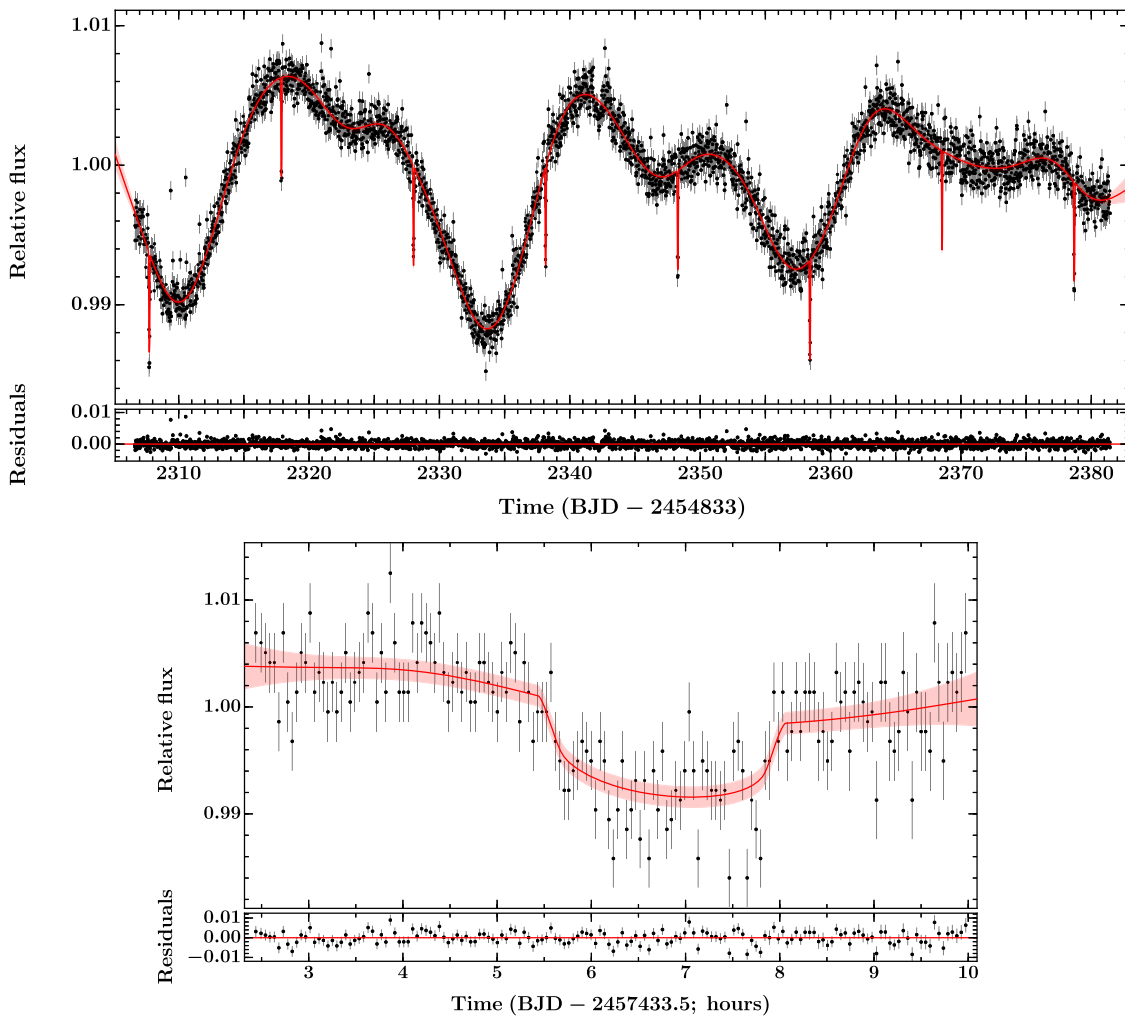


Figure 3. *K2* (top) and USNO (bottom) light curves of JS 183 (black) with the GP-transit model A (red). The *K2* light curve here is the same as the systematics-corrected PDC version shown in Figure 1. The red line and pink shaded region show the mean and 2σ confidence interval of the predictive posterior distribution of the GP-transit model. The USNO observations cover the transit 22 orbital periods later than the last event seen in the *K2* data.

Table 2
RV Observation of JS 183 with HIRES

Epoch UT Date	Spectral Range	S/N	RV Value (km s^{-1})	RV Error (km s^{-1})
1997 Dec 06 15:02:32	6300–8725 \AA	8	34.72	0.77
2015 Dec 24 15:55:01	4800–9200 \AA	21	34.24	0.33
2015 Dec 29 16:12:14	4800–9200 \AA	8	35.76	0.36
2016 May 20 07:22:30	4800–9200 \AA	28	36.18	0.35
2016 Dec 22 14:55:18	4800–9200 \AA	25	34.14	0.27
2016 Dec 26 13:01:33	4100–8000 \AA	9	36.72	1.11

reported to be $\sim 7 \text{ km s}^{-1}$. In Section 4.3 we use the six RV measurements reported here to set an upper limit on the mass of the transiting planet.

4. Results

4.1. Transit Model

Since we do not have dynamical confirmation of this planet from RV detection of the signal, we have taken two separate approaches to the analysis of the photometric observations, presented in the next two subsections. The consistent results of

the two approaches provide additional evidence for the reliability of the overall system properties.

4.1.1. Primary Analysis: GP-transit Model

The *K2* light curve of JS 183 is shown in Figure 1 and displays evolving starspot modulation with an amplitude of $\sim 2\%$ and a period of ~ 24 days. To account for the effect of this stellar variability across each transit, we simultaneously model the out-of-transit variations at the same time as fitting for the transit parameters. We therefore model the full light curve as the sum of a GP plus transit model (hereafter GP-transit model). The transit component is based on the model presented in Irwin et al. (2011), which is a modified version of the (JKT) EBOP family of models, but which uses the analytic method of Mandel & Agol (2002) for the quadratic limb-darkening law. The GP component, which is used to describe the out-of-transit variability, is based on the *george* package (Ambikasaran et al. 2014; Foreman-Mackey et al. 2014). For the *K2* light curve, the GP component is a quasi-periodic exponential-sine-squared kernel, which is essentially a periodic kernel that is allowed to evolve over time, i.e., mimicking evolving starspot modulation.

Table 3
Priors on System Parameters for Analysis in Section 4.1.1

Case	Eccentricity	Stellar Density (g cm^{-3})	Effective Temperature (K)	$\log g$
A (eccentric, empirically constrained SD ^a)	$\mathcal{U}(0, 1.0)$	$7.266_{-1.431}^{+1.877}$	$\mathcal{N}(\mu = 3350, \sigma = 50)$	$\mathcal{N}(\mu = 4.79, \sigma = 0.08)$
B (eccentric, SED-constrained SD)	$\mathcal{U}(0, 1.0)$	$3.703_{-2.534}^{+8.035}$	$\mathcal{N}(\mu = 3350, \sigma = 50)$	$\mathcal{N}(\mu = 4.5, \sigma = 0.5)$
C (eccentric, unconstrained SD)	$\mathcal{U}(0, 1.0)$	$\mathcal{U}(0, 160)$
D (circular, unconstrained SD)	δ	$\mathcal{U}(0, 160)$

Notes. $\mathcal{U}(a, b)$ —uniform density with a minimum a and maximum b . $\mathcal{N}(\mu, \sigma)$ —normal density with mean μ and standard deviation σ . δ —Dirac’s delta function.
^a SD = stellar density.

In addition to the *K2* discovery light curve, we use the USNO light curve described in Section 3.2. The single-night observation is not long enough to clearly see the evolving starspot modulation displayed in the *K2* light curve. Instead, the dominant variations display a relatively rough behavior over short ($\lesssim 1$ hr) timescales. Accordingly, we opt for a Matern-3/2 kernel in our GP model, as its covariance properties are more suited to the observed behavior.

We simultaneously modeled the *K2* and USNO light curves using our *GP-transit* model, with the parameter space explored through the affine-invariant Markov chain Monte Carlo (MCMC) method, as implemented in `EMCEE` (Foreman-Mackey et al. 2013). This model will be presented in detail in E. Gillen et al. (2017, in preparation). We ran the MCMC for 50,000 steps with each of 144 “walkers” and derived parameter distributions from the last 25,000 steps of each chain (after thinning each chain from inspection of the autocorrelation lengths for each parameter). In addition, the *K2* model was supersampled to 1-minute cadence.

Since we do not have strong prior information about the eccentricity of this orbit, we opted to apply four different models to this system. These models are presented in Table 3 and differ only in their eccentricity, effective temperature, and surface gravity priors, the latter two giving different priors on the stellar density: (A) an eccentric orbit with a stellar density prior from the empirical relations of Mann et al. (2016a) (see Section 4.2), (B) an eccentric orbit with a stellar density prior from the SED fitting (again see Section 4.2), (C) an eccentric orbit with an uninformative stellar density prior, and (D) a circular orbit with an uninformative stellar density prior. Model A is our main model. We then test this stellar density prior first by relaxing it slightly in model B and then by relaxing it fully with an uninformative prior in model C. Finally, in model D, we keep the uninformative stellar density prior but force the orbit to circular to investigate the effect of eccentricity.

The effective temperature and surface gravity priors in models A and B naturally give rise to priors on the limb-darkening coefficients. These were computed using the `LDTK` toolkit (Parviainen 2015), which allows us to propagate the uncertainties in these stellar parameters (and the metallicity $Z = 0.1 \pm 0.1$) through the PHOENIX stellar atmosphere models (Husser et al. 2013) into our coefficients. The uncertainties on the limb-darkening coefficients were then inflated by a factor of 50 to account for differences between model grids. In the light curve modeling, the limb-darkening parameterization follows the triangular sampling method of Kipping (2013; see that paper for the relationship between the “ q ” parameters plotted in Figure 6 and standard quadratic limb-darkening coefficients). Uninformative priors were used on all other transit parameters.

Using models A–D, we can explore the information content of the data, how our priors affect our results, and the confidence with which we can characterize this system. The individual models are presented and compared below.

4.1.1.1. Individual Models: Investigating the Effect of Eccentricity and Assumed Stellar Density

Given that the planet orbital period lies close to an integer multiple of the *K2* cadence and that the USNO light curve is of modest precision, the eccentricity of the orbit is unlikely to be well constrained from these data alone. As we believe the empirically determined stellar density constraint to be well-founded, we opt to use model A (eccentric orbit with a stellar density constraint from empirical relations) as the main model discussed here, but we also present results from the other three for comparison and to investigate the effect of our assumptions.

Figure 3 shows the full *K2* and USNO light curves along with the *GP-transit* model A. The model is an acceptable fit to the large-scale structure of both light curves. In the *K2* case, the GP model predicts a stellar rotation period of 23.8 days and is able to reproduce the evolving shape of the modulation. For the USNO light curve, the GP favors a smooth model for the out-of-transit variations due to the observational uncertainties, even though apparent correlations can be seen in the residuals. The significance of these variations (as well as lower-level ones present in the *K2* light curve) are investigated at the end of this section. The top row of Figure 4 shows the model A transit fits to both the *K2* and USNO light curves (left and right, respectively). In the *K2* panel, the effect of the orbital period being close to an integer multiple of the cadence can be seen. Table 4 presents the parameters of model A (leftmost results column), and Figure 5 presents the 2D contours and 1D histograms of the transit parameter MCMC chains from which the posteriors reported in Table 4 are derived. There are significant correlations between the parameters of interest, as expected given that we only have photometric data of the transit (i.e., no secondary eclipse or RVs). Allowing an eccentric orbit drives most of the observed correlations: fixing the orbit to circular removes the correlations of interest, barring those between the cosine of the inclination ($\cos i$) and the radius sum ($(R_p + R_*)/a$). The correlations arise from the fact that small changes in a given parameter can be effectively masked by corresponding changes in one or more others without significant modification to the transit shape.

We now compare the four different models to investigate the effect of our assumptions about the eccentricity and stellar density. The four rows of Figure 4 show (in descending order) the fits of models A, B, C, and D. All models are able to reproduce the observed transit shapes within the observational uncertainties, even though they have different shapes and

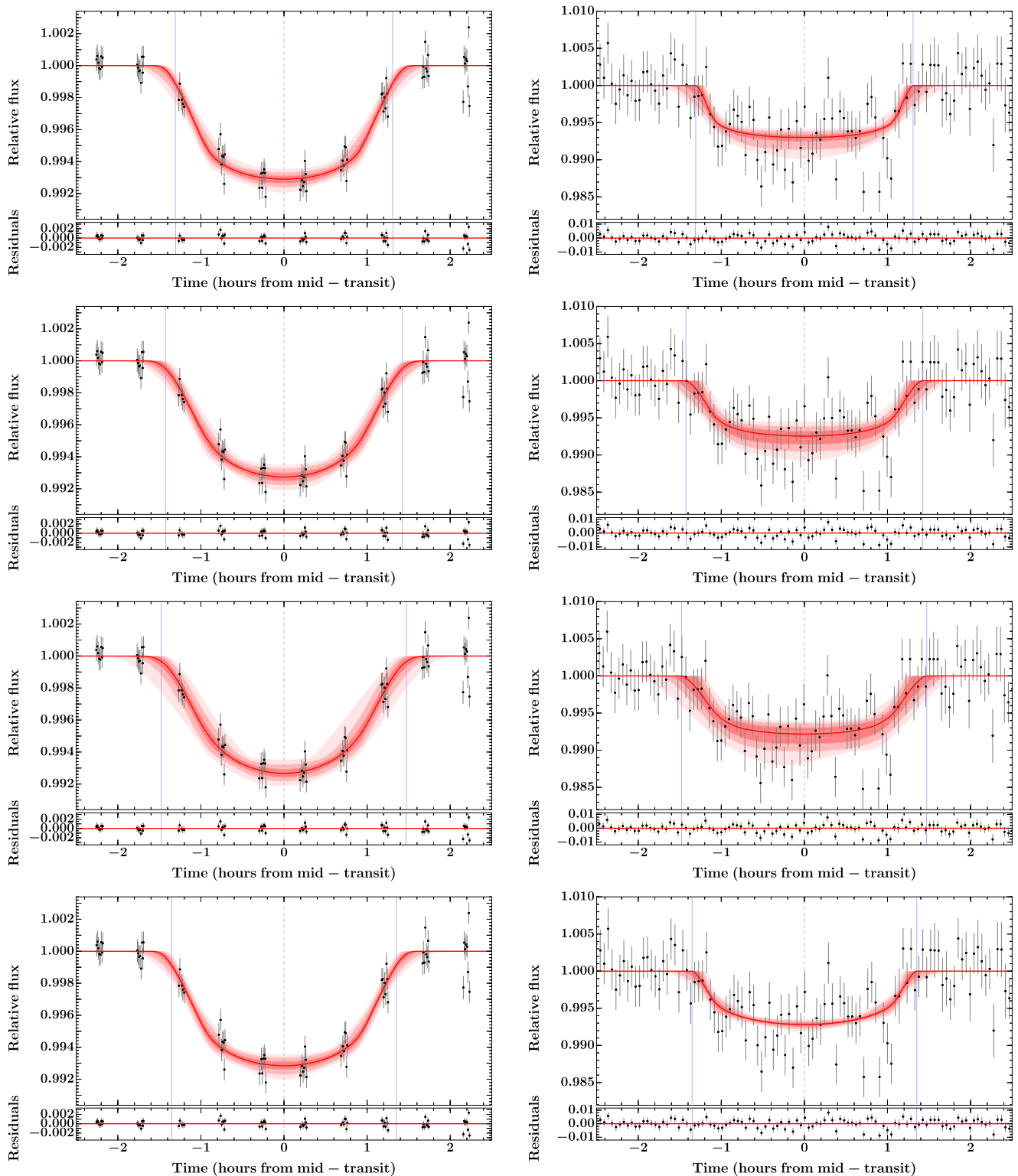


Figure 4. Phase-folded *K2* (left column) and USNO (right column) light curves, zoomed in around transit (black points), showing the GP-transit model fits (red). The light curves have been detrended with respect to the GP models (i.e., stellar variability and large-scale systematics). The red line and pink shaded regions indicate the median and 1σ , 2σ , and 3σ confidence regions of the GP-transit model. The vertical dashed and solid blue lines represent the transit center and first and fourth contacts, respectively. The *K2* model has been integrated to the 30-minute observational cadence, whereas the USNO model is not integrated given the short exposure times of the USNO data. Rows, top to bottom: model A (eccentric orbit, stellar density prior from empirical relations), model B (eccentric orbit, stellar density prior from the SED fitting), model C (eccentric orbit, uninformative stellar density prior), and model D (circular orbit, uninformative stellar density prior).

durations. These transit models are integrated to the *K2* cadence. To highlight the effect of this observational cadence on the depicted transit models, Figure 6 shows the unintegrated

transit of model A (red line and shaded regions) and the integrated model predictions for the times of observation (blue points).

Table 4
Parameters of the Different Light Curve Models Applied to JS 183

Parameter	Symbol	Unit	Value			
			Model A	Model B	Model C	Model D
Transit Parameters						
Sum of radii	$(R_*+R_p)/a$		$0.0339^{+0.0061}_{-0.0022}$	$0.050^{+0.020}_{-0.013}$	$0.069^{+0.026}_{-0.020}$	$0.0403^{+0.0175}_{-0.0062}$
Radius ratio	R_p/R_*		$0.0786^{+0.0086}_{-0.0026}$	$0.0852^{+0.0097}_{-0.0084}$	$0.0887^{+0.0097}_{-0.0113}$	$0.0794^{+0.0084}_{-0.0040}$
Orbital inclination	i	°	$89.25^{+0.53}_{-0.61}$	88.0 ± 1.6	86.4 ± 4.2	$88.82^{+0.82}_{-1.30}$
Orbital period	P	days	10.134589 ± 0.000084	10.134590 ± 0.000098	10.134603 ± 0.000102	10.134588 ± 0.000094
Time of transit center	T_{center}	BJD	$2,457,282.6279 \pm 0.0011$	$2,457,282.6279 \pm 0.0015$	$2,457,282.6281 \pm 0.0020$	$2,457,282.6278 \pm 0.0012$
	$\sqrt{e} \cos \omega$		0.02 ± 0.43	0.01 ± 0.52	-0.03 ± 0.6	...
	$\sqrt{e} \sin \omega$		$-0.29^{+0.20}_{-0.28}$	-0.04 ± 0.42	$0.28^{+0.38}_{-0.50}$...
Eccentricity	e		$0.24^{+0.27}_{-0.18}$	$0.27^{+0.27}_{-0.19}$	$0.46^{+0.21}_{-0.30}$...
Longitude of periastron	ω	°	$-76.8^{+53.0}_{-69.7}$	-10.0 ± 130.0	58.0 ± 75.0	...
K2 linear LD coefficient	u_{K2}		0.456 ± 0.082	0.67 ± 0.26	0.88 ± 0.38	0.60 ± 0.27
K2 nonlinear LD coefficient	u'_{K2}		0.24 ± 0.20	0.09 ± 0.29	-0.11 ± 0.39	0.07 ± 0.34
USNO linear LD coefficient	u_{USNO}		0.304 ± 0.079	0.27 ± 0.22	$0.28^{+0.31}_{-0.20}$	0.60 ± 0.27
USNO nonlinear LD coefficient	u'_{USNO}		0.21 ± 0.22	$0.16^{+0.31}_{-0.22}$	$0.13^{+0.32}_{-0.23}$	0.07 ± 0.34
Out-of-transit Variability Parameters						
K2 amplitude	A_{K2}	%	$0.230^{+0.058}_{-0.042}$	$0.226^{+0.056}_{-0.042}$	$0.222^{+0.057}_{-0.041}$	$0.226^{+0.054}_{-0.041}$
K2 timescale of SqExp term	$l_{\text{SE } K2}$	%	156.2 ± 3.4	156.2 ± 3.3	155.6 ± 3.3	156.3 ± 3.3
K2 scale factor of ExpSine2 term	$\Gamma_{\text{ESS } K2}$	days	0.484 ± 0.090	$0.491^{+0.092}_{-0.086}$	0.494 ± 0.092	0.490 ± 0.088
K2 period of ExpSine2 term	$P_{\text{ESS } K2}$	days	23.83 ± 0.29	23.84 ± 0.28	23.85 ± 0.31	23.83 ± 0.27
K2 white-noise term	σ_{K2}	%	1.371 ± 0.017	1.371 ± 0.018	1.371 ± 0.017	1.371 ± 0.017
USNO amplitude	A_{USNO}	%	0.36 ± 0.18	0.32 ± 0.18	0.31 ± 0.20	0.37 ± 0.17
USNO timescale	l_{USNO}	days	$5.0^{+2.6}_{-2.0}$	5.9 ± 2.7	6.4 ± 2.6	5.0 ± 2.4
USNO white-noise term	σ_{USNO}	%	1.167 ± 0.071	$1.175^{+0.079}_{-0.069}$	$1.175^{+0.075}_{-0.068}$	$1.173^{+0.071}_{-0.065}$

Note.

^a LD = limb darkening.

Figure 7 presents the posterior parameter distributions of the four GP-transit models. As expected, the period and ephemeris are essentially insensitive to the choice of model and underlying assumptions. As previously mentioned, the limb-darkening coefficients of models A and B are theoretically constrained given the assumed stellar temperature, surface gravity, and cluster metallicity, whereas they are unconstrained in models C and D; the differences can be seen in the limb-darkening panels of Figure 7. In the distributions for the radius sum ($(R_p+R_*)/a$), radius ratio (R_p/R_*), inclination (i), and the combination terms $\sqrt{e} \cos \omega$ and $\sqrt{e} \sin \omega$, we see the effect of our assumptions about the eccentricity and stellar density. First, the stellar density: this essentially places a prior on the transit duration, which in turn constrains the radius ratio, radius sum, and $\sqrt{e} \sin \omega$ (and to lesser extents $\sqrt{e} \cos \omega$ and the orbital period P). Most importantly, model A (black), which places a tight constraint on the stellar density, constrains the transit duration such that the model favors a single-peaked radius ratio distribution around $R_p/R_* \sim 0.075$ – 0.08 . Relaxing the constraint on the stellar density (models B and C; orange and blue, respectively) allows the model to explore an additional family of solutions composing a larger planet-to-star radius ratio (and correspondingly these models explore a larger range of inclinations, radius sums, and eccentricities to remain

consistent with the observed fluxes). The effect of eccentricity can be investigated by comparing models C and D (blue and green, respectively). Forcing the orbit to be circular has a similar effect to placing a tight constraint on the stellar density: model D favors a single-peaked radius ratio distribution and has tighter posterior distributions for the radius sum and inclination than models B and C.

The GP hyperparameters are mainly insensitive to the chosen model. For the K2 light curve, the amplitude (A_{K2}), period ($P_{\text{ESS } K2}$), and white-noise term (σ_{K2}) are well constrained by the data, but the scale factor ($\Gamma_{\text{ESS } K2}$) and evolutionary timescale ($l_{\text{SE } K2}$) have Gaussian priors that essentially define their posterior distributions. The evolutionary timescale is related to the half-life of the active regions that are responsible for the observed modulation pattern; however, the exact nature of this relationship is not firmly established. It is worth noting that data covering two evolutionary periods are needed to robustly constrain this parameter, so it is not surprising that it is not well constrained in this case. However, while the evolutionary timescale and scale factor affect the other GP hyperparameters, they do not affect the final transit parameters significantly. For the USNO light curve, the GP amplitude (A_{USNO}) and timescale (l_{USNO}) hyperparameters are not well determined; the differences in the timescale posteriors arise

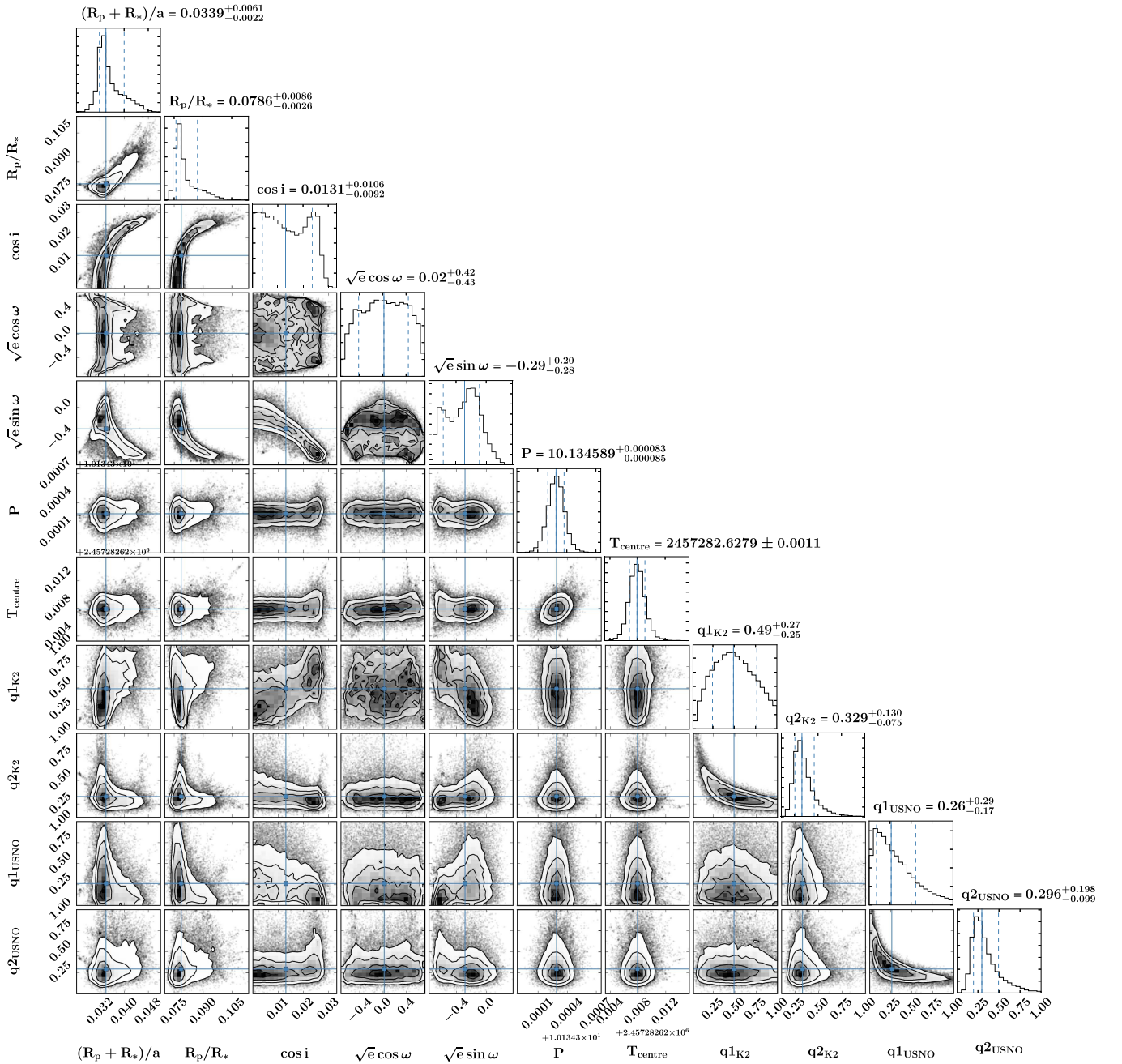


Figure 5. 2D contours and 1D histograms of the MCMC chains for the GP-transit model A, showing the transit parameters only of both the K2 and USNO light curve models. On the 2D plots, blue squares show the median values and black contours represent 1σ , 2σ , and 3σ confidence intervals. On the histograms, solid and dotted vertical lines show the median and $\pm 1\sigma$ intervals, respectively. For limb darkening we use the method of Kipping (2013), and we quote the “ q ” parameters from that formulation here. This figure was built with `corner.py` (Foreman-Mackey 2016).

from the tightness of the different transit model fits and are therefore driven by the stellar density and eccentricity constraints.

4.1.1.2. Investigating the Residual Variations in the K2 and USNO Light Curves

K2: The model presented above for the K2 light curve seeks to explain the large-scale structure. While it is an acceptable fit to the data, zooming in on small sections of the light curve reveals small-amplitude, short-timescale variations, which could arise from low-level stellar variations or residual systematics. Arguably, adding another GP into the model

might account for these, but there would be a lot of flexibility in such a composite GP model, and it is not clear that the residual variations are significant throughout the majority of the light curve. Therefore, to test the significance of these residual variations, we first detrended the light curve with respect to the smoothly varying starspot modulations and then modeled the residual light curve using a Matern-3/2 kernel in our GP-transit model (as previously discussed, this kernel displays a relatively rough behavior, which is suited to the observed residual systematics). It appears as though the information content of the residual light curve is not sufficient to support the additional treatment of the Matern-3/2 kernel. The GP model favors a very small amplitude and either a long timescale over which to

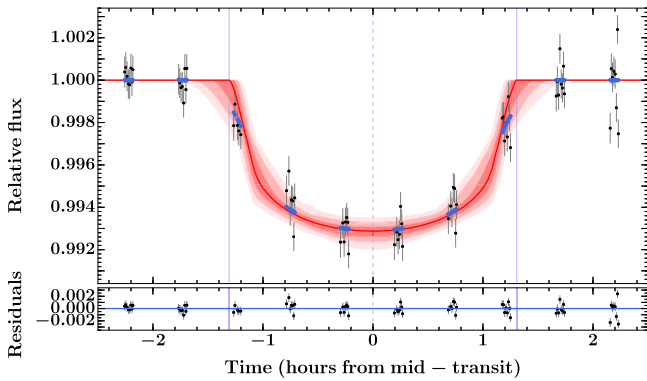


Figure 6. Unintegrated K2 transit model for model A. The light curve has been detrended with respect to the GP model. The red line and pink shaded regions indicate the median and 1σ , 2σ , and 3σ confidence regions of the unintegrated GP-transit model. The blue points show the integrated model predictions for the times of observation. The vertical dashed and solid blue lines represent the transit center and first and fourth contacts, respectively.

vary or a very short one, depending on the initial guess for the input scale. Neither of these is suited to the observed residuals, which have timescales of a few hours, and which are at times clearly observed above the noise. We therefore did not use a more sophisticated GP kernel for the K2 light curve.

USNO: The residuals of the USNO model are clearly seen in the bottom panel of Figure 3. The mean GP model smoothly varies over a relatively long timescale, in contrast to parts of the light curve that show variations over $\lesssim 1$ hr timescales. To assess the significance of these variations, we reran our model and used the GP itself to estimate the full observational uncertainties (rather than simply allowing it to inflate the uncertainties if required). This second model converges on the same variability and transit parameter values as presented above, which suggests that the information content of the light curve is not sufficient to warrant smaller uncertainties; accordingly, we did not investigate the observed variations further.

It is worth noting, however, that the validity of the observational uncertainties, and hence the analysis above, is subject to the choice of model. Here, the GP model attempts to find the simplest way of explaining the data, *given our choice of covariance kernel*, and in doing so may opt to increase the uncertainties on each data point rather than the complexity of the chosen family of models if the data set *as a whole* is unable to support the additional complexity. Accordingly, in model A (presented in Section 4.1.1), the GP opted to slightly inflate the uncertainties by factors of ~ 1.37 and 1.17 for the K2 and USNO light curves, respectively (see Table 4).

4.1.2. Sanity Check: Independent K2 Light Curve Analysis

We carry out a second independent light curve analysis to ensure the robustness of our primary analysis. This analysis uses the K2SC-detrended PDC-MAP light curve and simplifies the approach by assuming white noise. The transits are modeled using PYTRANSIT (Parviainen 2015) with a quadratic Mandel–Agol model, and EMCEE is used for posterior sampling, as in the main analysis (Section 4.1.1). The files associated with this analysis can be found from GitHub at <https://github.com/hpparvi/prae1b>.

This analysis consider four cases for orbital eccentricity, stellar density, and $\log g$ (assuming a stellar radius of

$0.43 R_{\odot}$), listed in Table 5. The sampling space is 10-dimensional, composed of the zero epoch, orbital period, planet–star area ratio, impact parameter, stellar density, $\sqrt{e} \cos \omega$, $\sqrt{e} \sin \omega$, two quadratic limb-darkening parameters, and average white-noise level. All the parameters except the eccentricity and $\log g$ have uninformative priors, and the limb darkening uses the parameterization described by Kipping (2013).

The posterior sampling starts by creating a parameter vector population of 100 walkers distributed uniformly inside the prior boundaries. We clump the population close to the global posterior maximum using the Differential Evolution global optimization algorithm implemented in PYDE¹⁵ (Parviainen 2016) and initialize the MCMC sampler with the clumped parameter vector population. The sampler is run over 15,000 iterations and then samples from every 100th iteration, after a burn-in set of 2000 iterations is selected to represent the posterior distribution. The thinning factor of 100 iterations was chosen by inspecting the autocorrelation lengths for individual parameters.

The results from the sanity check analyses are shown in Figure 8, and they agree with the primary analysis. One small difference between the two analyses is that the main analysis finds a broader and near-bimodal distribution for the planet/star radius ratio. We believe that this is because the main analysis uses GPs, whereas the analysis in this section assumes white noise. When using GPs, the transit shape does not constrain the parameter space as strongly, and that additional freedom allows for a larger variety of possible solutions. In the end, we do not believe that this difference represents a challenge to our final system parameters.

4.2. SED Analysis

We fit a grid of BT-SETTL stellar atmosphere models (Allard et al. 2012) to the available *ugrizJHK_s* + WISE 1–3 catalog photometry, spanning the wavelength range $0.35\text{--}12\ \mu\text{m}$ (summarized in Table 6). The reported uncertainties on the Sloan Digital Sky Survey (SDSS) *griz* photometry are very small (~ 0.005 mag), so we rounded up these photometric uncertainties to 0.05 mag to account for photometric variability due to modest activity in this source, as well as zero-point uncertainties of ≈ 0.02 mag in the SDSS photometry. The free parameters of the fit are T_{eff} , $\log g$, $[\text{Fe}/\text{H}]$, and A_V ; for the latter we adopted a maximum possible value of 0.085 mag based on the full line-of-sight extinction from the Schlegel et al. (1998) dust maps. We interpolate the model grid by 10 K T_{eff} from the native gridding of 100 K. We do not interpolate more finely than the native gridding of 0.5 dex in $\log g$ and $[\text{Fe}/\text{H}]$ because broadband SED fitting is much less sensitive to these parameters compared with T_{eff} .

The resulting best-fit parameters are $T_{\text{eff}} = 3350 \pm 50$ K, $A_V = 0.000^{+0.085}_{-0.000}$, $\log g = 4.5 \pm 0.5$, $[\text{Fe}/\text{H}] = 0.0 \pm 0.5$. The fit is shown in Figure 9, with a reduced χ^2 of 6.1. The uncertainties in the fit parameters are estimated according to the usual criterion of $\Delta\chi^2 = 4.72$, relative to the best fit, for four fit parameters (e.g., Press et al. 1992), where we first rescaled the χ^2 so as to make the reduced χ^2 of the best fit equal to 1. This is equivalent to inflating the measurement errors by a constant factor and has the effect of increasing the parameter

¹⁵ <https://github.com/hpparvi/PyDE>

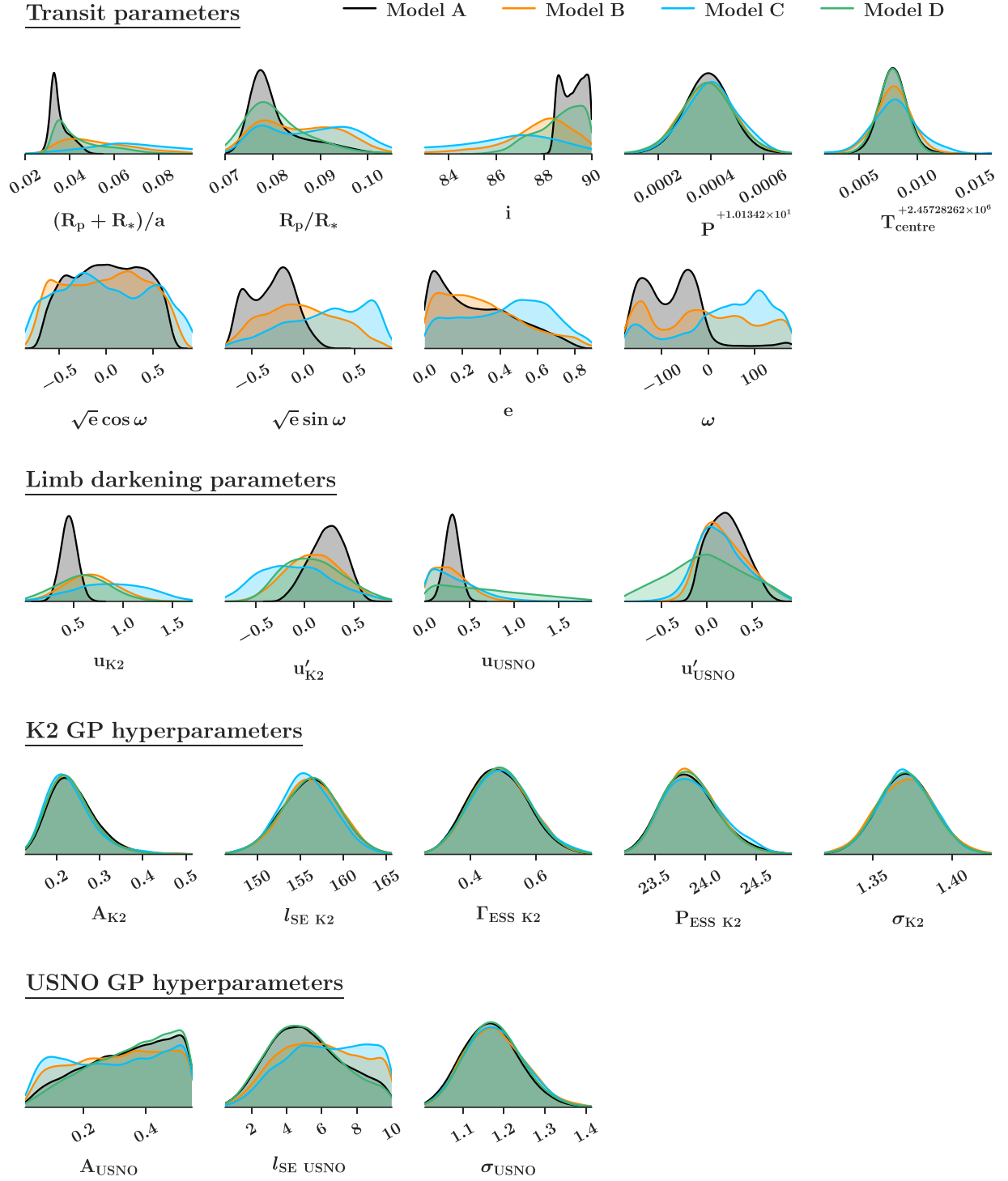


Figure 7. Posterior parameter distributions of the four GP-transit models: A (black; main model), B (orange), C (blue), and D (green). The transit parameters, limb-darkening coefficients, and GP hyperparameters are grouped from top to bottom.

Table 5
Priors on System Parameters for Analysis in Section 4.1.2

Case	Eccentricity	Stellar Density (g cm^{-3})	$\log g$
A (constrained $\log g$ 2)	$\mathcal{U}(0, 0.9)$	$\mathcal{U}(0.5, 15)$	$\mathcal{N}(\mu = 4.81, \sigma = 0.08)$
B (constrained $\log g$ 1)	$\mathcal{U}(0, 0.9)$	$\mathcal{U}(0.5, 15)$	$\mathcal{N}(\mu = 4.5, \sigma = 0.5)$
C (eccentric, unconstrained)	$\mathcal{U}(0, 0.9)$	$\mathcal{U}(0.5, 15)$	$\mathcal{U}(3, 8)$
D (circular)	δ	$\mathcal{U}(0.5, 15)$	$\mathcal{U}(3, 8)$

Note. $\mathcal{U}(a, b)$ —uniform density with a minimum a and maximum b . $\mathcal{N}(\mu, \sigma)$ —normal density with mean μ and standard deviation σ . δ —Dirac’s delta function.

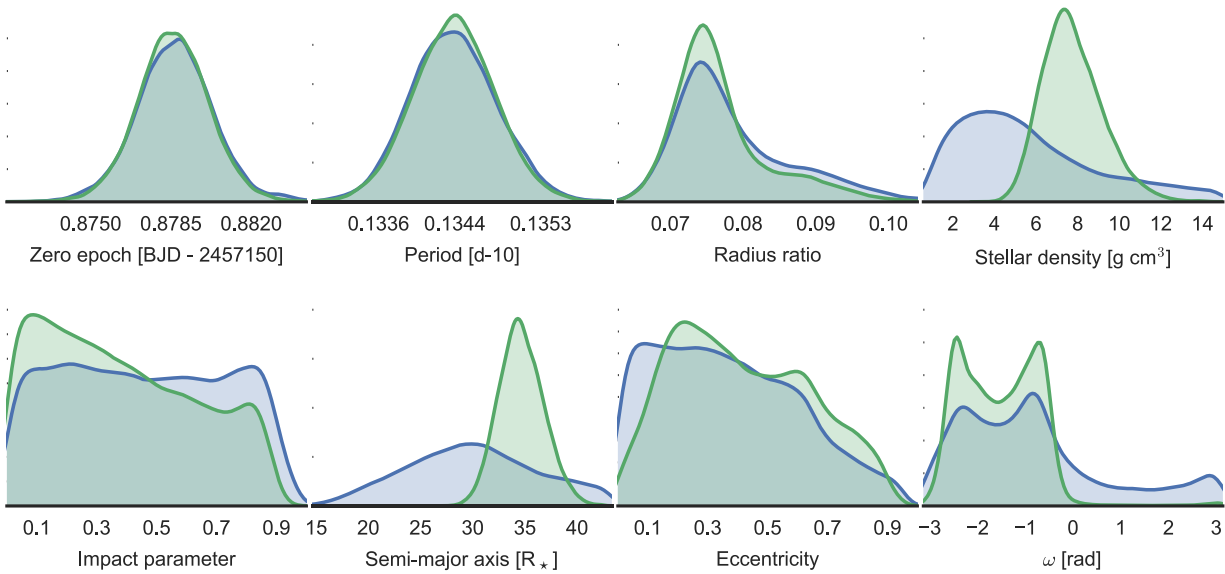


Figure 8. Parameter posteriors from the second K2 light curve analysis cases A (green) and B (blue), showing the impact of different priors on $\log g$ on the parameter estimates.

Table 6
Catalog Photometry of JS 183

Bandpass	Mag.	Mag. Err.	Source
<i>u</i>	20.704	0.053	SDSS9
<i>g</i>	18.025	0.006	SDSS9
<i>r</i>	16.635	0.006	SDSS9
<i>i</i>	15.370	0.005	SDSS9
<i>z</i>	14.696	0.005	SDSS9
<i>J</i>	13.312	0.021	2MASS
<i>H</i>	12.738	0.024	2MASS
<i>K</i>	12.474	0.021	2MASS
W1	12.323	0.024	ALLWISE
W2	12.211	0.030	ALLWISE
W3	11.240	0.356	ALLWISE

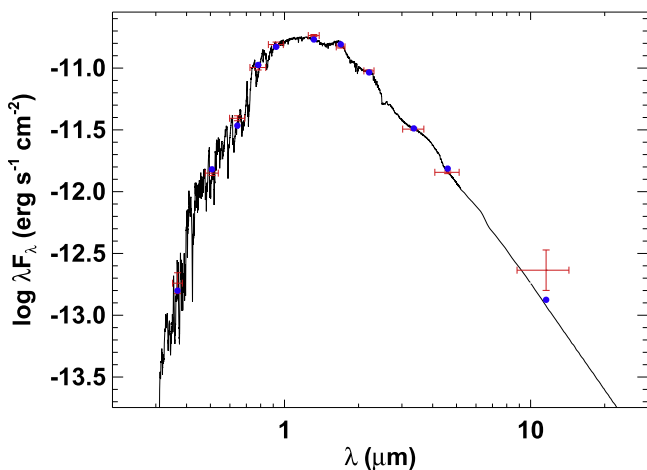


Figure 9. SED fit with BT-SETTL atmosphere model. Red symbols are the catalog photometry; blue symbols are the corresponding model fluxes.

uncertainties accordingly. The T_{eff} from our SED fit is consistent with the previously reported M3.5 spectral type (Adams et al. 2002) to within ~ 0.5 spectral subtype.

We can use the fitted SED models to compute a bolometric flux at Earth, again according to the $\Delta\chi^2$ criterion above. This gives $F_{\text{bol}} = 2.10 \pm 0.09 \times 10^{-11} \text{ erg s}^{-1} \text{ cm}^{-2}$. Note that this F_{bol} and its uncertainty are robust because the model fit is essentially an interpolation of the observed fluxes that span the majority of the SED. This F_{bol} , together with the nominal cluster distance of $182 \pm 6 \text{ pc}$ (van Leeuwen 2009) and the best-fit T_{eff} , then permits a calculation of the stellar radius via the Stefan–Boltzmann relation, giving $R = 0.44 \pm 0.03 R_{\odot}$. The radius uncertainty includes the uncertainties on the bolometric flux, the parallax distance, and T_{eff} , in quadrature.

This is somewhat larger than the radius predicted from the empirical $T_{\text{eff}}-R$ relation of Mann et al. (2016a), which gives $R = 0.31 \pm 0.04 R_{\odot}$. However, the Praesepe cluster has been reported to be metal-rich, with $[\text{Fe}/\text{H}] \approx 0.1$, but in some cases reported to be as high as $[\text{Fe}/\text{H}] = 0.27 \pm 0.10$ (Pace et al. 2008). Using this range of $[\text{Fe}/\text{H}]$ with the $T_{\text{eff}}-[\text{Fe}/\text{H}]-R$ relation of Mann et al. (2016a) predicts $R = 0.37 \pm 0.03 R_{\odot}$. Finally, adopting instead the $M_{K_S}-[\text{Fe}/\text{H}]-R$ relation of Mann et al. (2016a), which those authors find has the tightest of all the empirical relations, gives $R = 0.42 \pm 0.01 R_{\odot}$, in good agreement with our measured value.

Finally, the star is reported both here and in Barrado y Navascués et al. (1998) (Section 2.3) to have a filled-in $\text{H}\alpha$ line, with $\text{EW}(\text{H}\alpha) \approx 0 \text{ \AA}$ indicating the presence of low-level chromospheric activity. Stassun et al. (2012) found that the $\text{H}\alpha$ EW is directly related to the degree of radius inflation in chromospherically active low-mass stars, and their empirical relations give a radius inflation of $\sim 6\%$ for $\text{EW}(\text{H}\alpha) = 0 \text{ \AA}$. Adjusting the Mann et al. (2016a) $M_{K_S}-[\text{Fe}/\text{H}]$ predicted radius for this amount of inflation and including the uncertainty in the Stassun et al. (2012) relation then gives a final predicted radius of $R = 0.44 \pm 0.02 R_{\odot}$, in excellent agreement with the bolometric radius value we measure above.

4.3. Planet Properties

Next, we seek to determine the physical properties of the planet. The planet radius is tied to the stellar radius via the transit radius ratio, and the planet mass is tied to the stellar mass via

Table 7
Final Properties of the JS 183 System

Property	Value	Uncertainty
M_*	$0.44 M_\odot$	$0.04 M_\odot$
R_*	$0.44 R_\odot$	$0.03 R_\odot$
T_{eff}	3350 K	50 K
$\log g_*$	4.82	0.06
[Fe/H]	0.1	0.1
R_{pl}	$0.32 R_J$	$0.02 R_J$
M_{pl}	$<1.67 M_J$...
T_{eq}	480 K	23 K
Age	$\sim 600^{\text{a}}$ Myr— $790 \pm 60^{\text{b}}$ Myr	

Notes.

^a Adams et al. (2002).

^b Brandt & Huang (2015).

the RV mass ratio. The host star’s radius we have determined above (Section 4.2) to be $R = 0.44 \pm 0.03 R_\odot$, consistent with the (activity-corrected) predicted radius from the empirical relations of Mann et al. (2016a). Similarly, we estimate the host star mass from the same empirical relations. Using the Mann et al. (2016a) relation for M_* versus M_{K_S} , we obtain an estimated mass of $0.44 \pm 0.04 M_\odot$, where the uncertainty includes both the photometric and distance uncertainties on M_{K_S} and the scatter in the empirical relation. This mass, together with the radius from above, then gives a stellar surface gravity of $\log g = 4.82 \pm 0.06$.

The ratio of the planet radius to the stellar radius is found to be 0.08, and with the measured stellar radius of $0.44 R_\odot$, that yields a planet radius of $0.32 \pm 0.02 R_J$. We can also calculate an estimated equilibrium temperature for the planet based on the ratio of the stellar radius to planet semimajor axis, stellar temperature, taking the orbit to be circular, and assuming a Bond albedo of 0.3 (similar to Neptune). With those assumptions, we find $T_{\text{eq}} = 480 \pm 23$ K. The full list of derived and calculated planet properties is listed in Table 7.

We have performed an analysis of our RV measurements in order to estimate an upper limit for the mass of the transiting planet. We have six RV measurements, and the standard deviation of these measurements is 1.08 km s^{-1} , which corresponds to a maximum mass for the planet of $6.7 M_{\text{Jup}}$ (assuming a zero eccentricity). However, in order to take the shape of the RV model into account, we have tested a circular-orbit model with seven free parameters, namely, the systemic RV (uniform prior between 30 and 40 km s^{-1}), orbital period, time of mid-transit and inclination (all three with Gaussian priors based on the light curve analysis), stellar mass (Gaussian prior according to the above estimation), and planet mass (with a uniform prior between 0 and 30 Jupiter masses). We have also included RV jitter (with uniform prior between 0 and 5 km s^{-1}) to account for possible additional sources of white noise. We used the EMCEE code (Foreman-Mackey et al. 2013) to explore the posterior distribution of the planetary mass based on the current data. We used 50 walkers and 5000 steps per walker. We then used a simple burn-in of half of the chains and merged all of them to get the final posterior distribution. This method is similar to that used in Grunblatt et al. (2016). The result of this analysis yields no detection of the planet (as expected from the RV uncertainties). However, it allows us to set an upper limit for the mass of the transiting object of $0.83 M_{\text{Jup}}$ at 99.7% confidence given the current data (assuming $e = 0$). The results of these tests are shown in Figure 10. Note that in this RV phase plot, the maximum expected RV displacement based on the transit model

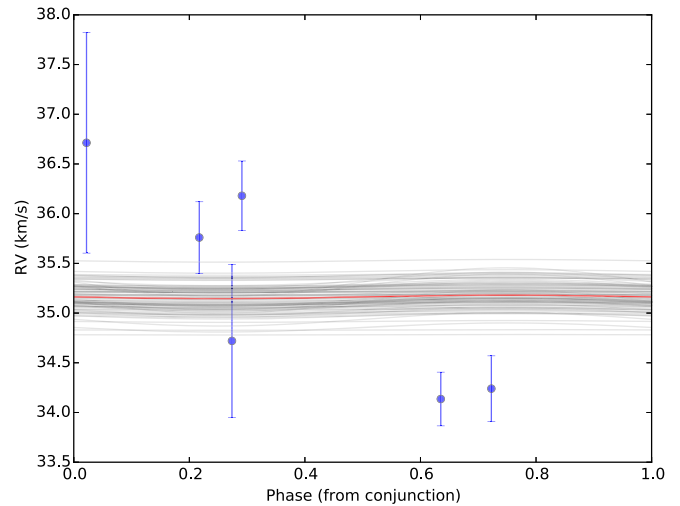


Figure 10. RV observations of JS 183 in blue, with various fits as described in the text superimposed. Gray lines represent the individual model fits, with the red line representing the model with parameters equal to the median of the marginalized posterior probabilities. With large errors compared to the expected RV amplitude, we do not detect the associated dynamical signal of the planet. Note that the transit observations predict negative RV variation at a phase of 0.25 and positive RV variation at a phase of 0.75. We are able to place a limit of $0.83 M_{\text{Jup}}$ at 99.7% confidence as the upper limit for any planet on the system, still well above the expected mass of the transiting planet detected by *K2*.

would occur at a phase of 0.75, opposite the offset of the RV observation at that phase, which therefore strongly constrains the allowable mass of the companion.

The planet orbiting JS 183 can therefore not yet be confirmed through RV detection of the stellar reflex motion. For a planet with a radius of about $0.32 R_J$, we would expect a mass of roughly $15 R_\oplus$ (see, e.g., Chen & Kipping 2016). For a host star with $M_* = 0.44 \pm 0.04 M_\odot$ and a circular orbit with a period of 10.134588 days, we would expect an RV semi-amplitude of about 0.008 km s^{-1} , far below the $\approx 0.3 \text{ km s}^{-1}$ errors of our HIRES RV observations (Table 2). Although the object would be detectable using current state-of-the-art precision RV techniques having $1\text{--}2 \text{ m s}^{-1}$ errors (see, e.g., Plavchan et al. 2015), the star is too faint in practice for these methods to be applied. In such cases, validation of the planet interpretation is typically undertaken either empirically or statistically. Empirical methods use a suite of observations that may be sensitive to detection of certain kinds of blend scenarios (e.g., O’Donovan et al. 2006) that could mimic the observed transit signal. Statistical methods can estimate the probability of various contaminating eclipsing binary scenarios given the source location on the sky relative to the modeled galactic field star population and assumptions regarding the mass function, binary fraction, and binary mass ratios (e.g., Morton 2014).

As we were writing this paper, we became aware of work by Obermeier et al. (2016) and Mann et al. (2017), who independently discovered and followed up the same *K2* time series data on EPIC 211916756. The thorough false-positive analysis presented in the Obermeier et al. (2016) paper need not be repeated here. From empirical considerations, no companions are detected in high spatial resolution imaging or in spectroscopy. From statistical considerations, a false-positive probability calculation rules out line-of-sight blended and bound hierarchical eclipsing binary systems. Remaining for consideration is the planet hypothesis.

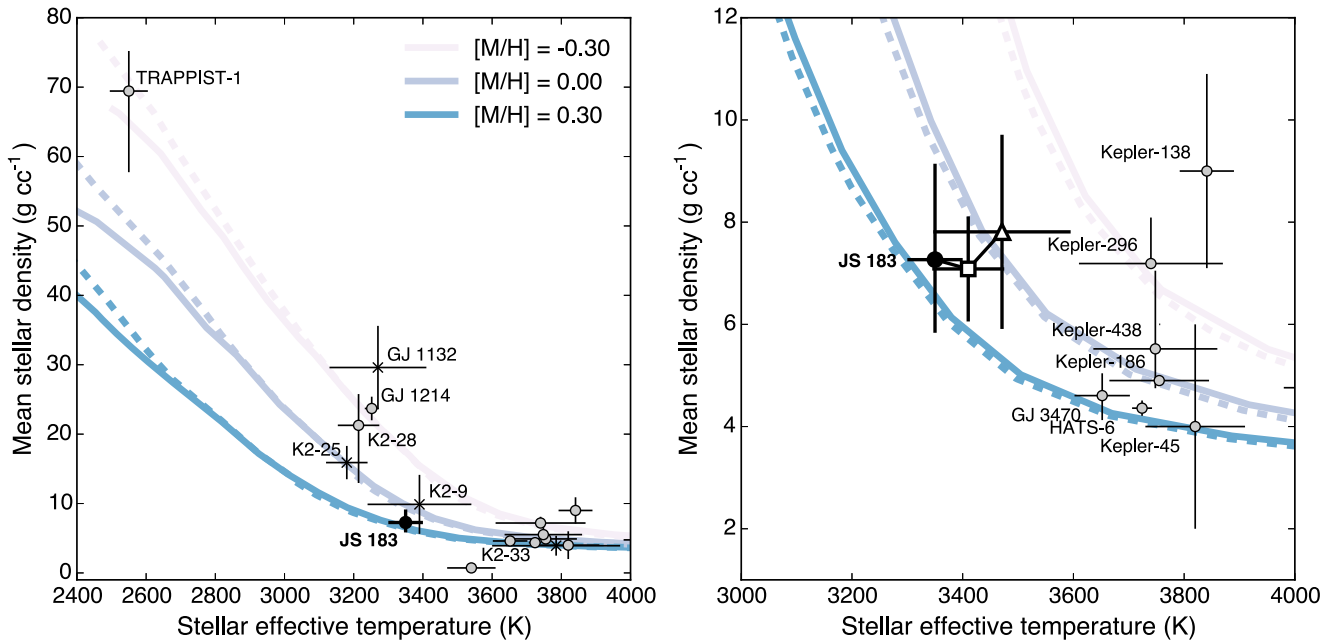


Figure 11. Left: late-type exoplanet host stars with well-determined stellar densities from transit fitting (filled markers) or through some combination of spectroscopy, models, and empirical relations (crosses). Underplotted are PARSEC v1.2S isochrones (Bressan et al. 2012) in the effective temperature–mean stellar density plane. Solid and dashed curves represent 600 Myr and 1 Gyr isochrones, respectively. Curve colors correspond to different metallicities. The solar-metallicity isochrone reproduces well the majority of transiting planet host stars cooler than 4000 K. At these cool temperatures, the mean stellar density is largely an indicator of metallicity and is relatively insensitive to age. The parameters for GJ 1214 are adopted from Anglada-Escudé et al. (2013). Preliminary transit fitting results of GJ 1132 suggest a lower stellar density than the value from empirical relations, which is plotted here (Z. Berta-Thompson 2017, private communication). The planet host K2-33 is a pre-main-sequence star (David et al. 2016b; Mann et al. 2016c) and thus substantially less dense than the field population. Right: enhanced view of the figure at left in the region around JS 183, only with those exoplanet hosts with densities constrained by transit fits. Three determinations for the parameters of JS 183 are indicated by the filled black circle (this work), open square (Mann et al. 2017), and open triangle (Obermeier et al. 2016). Notably, a supersolar-metallicity isochrone best matches the parameters of JS 183, consistent with the enhanced metallicity of the Praesepe cluster. Exoplanet host star data were culled from the NASA Exoplanet Archive, but mean stellar densities were taken from the transit fitting results of the primary references listed in the Exoplanet Archive, wherever reported.

5. Discussion

For low-mass stars, metallicity substantially affects the radius of the star (e.g., Mann et al. 2016a). Since the planet radius as obtained from the transit depends directly on the stellar radius, its precision is limited by the precision of the stellar radius, and hence metallicity. In general, cluster stars such as JS 183 have better-constrained metallicities than field stars, given the ability to study a large population that is presumed to be chemically homogeneous.

To date, there are more than 2500 unique hosts to confirmed exoplanets, but only 100 with effective temperatures ≤ 4000 K. Of these, only 16 have reliable mean stellar densities determined from either transit fitting or detailed stellar characterization and reported in the NASA Exoplanet Archive.¹⁶ We examine this complete sample of late-type hosts to confirmed transiting exoplanets in Figure 11. The figure shows that the higher metallicity of JS 183 leads to a larger radius and thus smaller stellar density than other transiting planet hosts of comparable temperature. For low-mass stars, which evolve slowly relative to higher masses, the mean stellar density is largely an indicator of metallicity and is relatively insensitive to age. Typically, as in this work, a stellar density determined from some combination of empirical relations and models is used as a prior in exoplanet transit fitting, due to the covariances between stellar density, e , and ω . However, if the orbital elements of an exoplanet are well constrained, the stellar density inferred from a transit light curve can be a powerful diagnostic of metallicity and test of stellar models at low masses; the technique of using exoplanet transits

to determine precise stellar densities is sometimes called asterodensity profiling (Kipping 2014).

Late-type transiting exoplanet hosts with temperatures higher than 3400 K are in general agreement with a field-age, solar-metallicity isochrone, using the PARSEC v1.2s models (Bressan et al. 2012). However, the majority of transiting exoplanet hosts with temperatures below 3400 K possess transit-derived stellar densities that are too large to be reproduced by the solar-metallicity models. While transit-derived stellar densities are often poorly constrained owing to the unknown orbital elements, transit fits tend to drive stellar density to *lower* values as a result of the aforementioned covariances and a bias favoring high-impact parameters or grazing transits (Kipping & Sandford 2016). There are hints of this bias apparent in Figure 8. Thus, e and ω may not be the only culprits explaining the larger dispersion in stellar densities for the coolest exoplanet hosts. It is possible that (1) stellar models may underpredict the densities of the coolest stars, or (2) some of the cool transiting exoplanet hosts have significantly subsolar metallicities. We presume that the latter explanation is unlikely, especially given the fact that the well-studied planet host GJ 1214 has a supersolar metallicity (Rojas-Ayala et al. 2012).

In comparison with other well-studied exoplanet hosts with a similar effective temperature, JS 183 has the lowest mean stellar density to date.¹⁷ The star’s low density is consistent with expectations of an inflated radius, due to the Praesepe cluster’s supersolar metallicity. The fact that JS 183’s spectral type of M3.5 is right near the stellar fully convective boundary

¹⁶ <http://exoplanetarchive.ipac.caltech.edu/>

¹⁷ K2-9 has a similar temperature and bulk density, though Schlieder et al. (2016) note a discrepancy between the transit-derived stellar density and the spectroscopically determined value that we show in the figure.

provides the intriguing suggestion that the models are performing well at masses/temperatures just above that boundary but performing poorly below that boundary, where the onset of full convection leads to additional challenges for low-mass stellar modeling.

The recent discoveries of short-period (<tens of days) Neptune-sized planets around young low-mass stars reveal planet radii significantly larger than the planets observed around field M dwarfs (Dressing & Charbonneau 2013, 2015), even after accounting for the trend of planet inflation with insolation. One possibility is that the young planets have not finished contracting and will eventually settle into the population of short-period super-Earths, a region of higher occurrence, as determined from *Kepler* statistics of field stars.

6. Summary and Conclusions

We have reported here the discovery of a Neptune-size planet transiting an M dwarf member of the Praesepe open cluster, also discussed by Obermeier et al. (2016) and Mann et al. (2017). Although we do not have a dynamical mass of the companion, we can constrain its mass to be planetary. This discovery adds to the small list of exoplanets found in open clusters and planetary companions of M dwarfs. The well-known age and metallicity of the Praesepe cluster give reliable values for those properties of the planet, which can be valuable for consideration of theoretical models of planet formation and evolution.

This system also features the best-determined radius for an M dwarf planet host and is only the third M dwarf planet host for which a reliable age is known via cluster membership. Indeed, with the lowest stellar density known among transiting planet hosts near the stellar fully convective boundary, JS 183 suggests that current stellar models are able to reproduce well its properties as arising from its supersolar metallicity, and further suggests that models remain challenged for stars with masses below the fully convective boundary.

J.P. would like to thank Ian Crossfield for useful discussions. T.D. is supported by an NSF Graduate Research Fellowship under grant DGE1144469. B.J.S.P. would like to thank Balliol College and the Clarendon Fund for their financial support of this work. S.A. and H.P. acknowledge funding from the Leverhulme Trust. S.A. received support from the UK Science and Technology Facilities Council (STFC). K.G.S. acknowledges partial support through NSF PAARE grant AST-1358862. J.L.-B. acknowledges support from the Marie Curie Actions of the European Commission (FP7-COFUND).

References

- Adams, J. D., Stauffer, J. R., Skrutskie, M. F., et al. 2002, *AJ*, 124, 1570
- Agüeros, M. A., Covey, K. R., Lemonias, J. J., et al. 2011, *ApJ*, 740, 110
- Aigrain, S., Hodgkin, S., Irwin, J., et al. 2007, *MNRAS*, 375, 29
- Aigrain, S., Parviainen, H., & Pope, B. J. S. 2016, *MNRAS*, arXiv:1603.09167
- Aigrain, S., & Pont, F. 2007, *MNRAS*, 378, 741
- Allard, F., Homeier, D., & Freytag, B. 2012, *RSPTA*, 370, 2765
- Ambikasaran, S., Foreman-Mackey, D., Greengard, L., Hogg, D. W., & O’Neil, M. 2014, arXiv:1403.6015
- Anglada-Escudé, G., Tuomi, M., Gerlach, E., et al. 2013, *A&A*, 556, A126
- Barrado y Navascués, D., Stauffer, J. R., & Randich, S. 1998, *ApJ*, 506, 347
- Beatty, T. G., & Gaudi, B. S. 2008, *ApJ*, 686, 1302
- Boesgaard, A. M., Roper, B. W., & Lum, M. G. 2013, *ApJ*, 775, 58
- Borucki, W. J., Koch, D., Basri, G., et al. 2010, *Sci*, 327, 977
- Boudreault, S., Lodieu, N., Deacon, N. R., & Hambly, N. C. 2012, arXiv:1207.4040
- Brandt, T. D., & Huang, C. X. 2015, *ApJ*, 807, 24
- Bressan, A., Marigo, P., Girardi, L., et al. 2012, *MNRAS*, 427, 127
- Brucalassi, A., Pasquini, L., Saglia, R., et al. 2014, *A&A*, 561, L9
- Burke, C. J., Gaudi, B. S., DePoy, D. L., & Pogge, R. W. 2006, *AJ*, 132, 210
- Chen, J., & Kipping, D. M. 2016, arXiv:1603.08614
- Christiansen, J. L., Jenkins, J. M., Caldwell, D. A., et al. 2012, *PASP*, 124, 1279
- Cutri, R. M., Skrutskie, M. F., van Dyk, S., et al. 2003, *yCat*, 2246, 0
- David, T. J., Conroy, K. E., Hillenbrand, L. A., et al. 2016a, *AJ*, 151, 112
- David, T. J., Hillenbrand, L. A., Petigura, E. A., et al. 2016b, *Natur*, 534, 658
- Delorme, P., Collier Cameron, A., Hebb, L., et al. 2011, *MNRAS*, 413, 2218
- Douglas, S. T., Agüeros, M. A., Covey, K. R., et al. 2014, *ApJ*, 795, 161
- Dressing, C. D., & Charbonneau, D. 2013, *ApJ*, 767, 95
- Dressing, C. D., & Charbonneau, D. 2015, *ApJ*, 807, 45
- Foreman-Mackey, D. 2016, *The Journal of Open Source Software*, 1, 2
- Foreman-Mackey, D., Hogg, D. W., Lang, D., & Goodman, J. 2013, *PASP*, 125, 306
- Foreman-Mackey, D., Hoyer, S., Bernhard, J., & Angus, R. 2014, george, v0.2.0, Zenodo, doi:10.5281/zenodo.11989
- Foreman-Mackey, D., Montet, B. T., Hogg, D. W., et al. 2015, *ApJ*, 806, 215
- Gould, A., Dorsher, S., Gaudi, B. S., & Udalski, A. 2006, *AcA*, 56, 1
- Grunblatt, S. K., Huber, D., Gaidos, E. J., et al. 2016, arXiv:1606.05818
- Hambly, N. C., Steele, I. A., Hawkins, M. R. S., & Jameson, R. F. 1995, *A&AS*, 109, 29
- Hartman, J. D., Gaudi, B. S., Holman, M. J., et al. 2009, *ApJ*, 695, 336
- Howard, A. W., Marcy, G. W., Bryson, S. T., et al. 2012, *ApJS*, 201, 15
- Howell, S. B., Sobek, C., Haas, M., et al. 2014, *PASP*, 126, 398
- Huber, D., Bryson, S. T., Haas, M. R., et al. 2015, arXiv:1512.02643
- Husser, T.-O., Wende-von Berg, S., Dreizler, S., et al. 2013, *A&A*, 553, A6
- Irwin, J. M., Quinn, S. N., Berta, Z. K., et al. 2011, *ApJ*, 742, 123
- Jones, B. F., & Stauffer, J. R. 1991, *AJ*, 102, 1080
- Kafka, S., & Honeycutt, R. K. 2006, *AJ*, 132, 1517
- Kipping, D. M. 2013, *MNRAS*, 435, 2152
- Kipping, D. M. 2014, *MNRAS*, 440, 2164
- Kipping, D. M., & Sandford, E. 2016, *MNRAS*, 463, 1323
- Kraus, A. L., & Hillenbrand, L. A. 2007, *AJ*, 134, 2340
- Lovis, C., & Mayor, M. 2007, *A&A*, 472, 657
- Malavolta, L., Nascimbeni, V., Piotto, G., et al. 2016, *A&A*, 588, A118
- Mandel, K., & Agol, E. 2002, *ApJL*, 580, L171
- Mann, A. W., Feiden, G. A., Gaidos, E., Boyajian, T., & von Braun, K. 2016a, *ApJ*, 819, 87
- Mann, A. W., Gaidos, E., Mace, G. N., et al. 2016b, *ApJ*, 818, 46
- Mann, A. W., Gaidos, E., Vanderburg, A., et al. 2017, *AJ*, 153, 64
- Mann, A. W., Newton, E. R., Rizzuto, A. C., et al. 2016c, arXiv:1604.06165
- Meibom, S., Torres, G., Fressin, F., et al. 2013, *Natur*, 499, 55
- Mermilliod, J.-C., & Mayor, M. 1999, *A&A*, 352, 479
- Mochejska, B. J., Stanek, K. Z., Sasselov, D. D., et al. 2005, *AJ*, 129, 2856
- Mochejska, B. J., Stanek, K. Z., Sasselov, D. D., et al. 2006, *AJ*, 131, 1090
- Mochejska, B. J., Stanek, K. Z., Sasselov, D. D., et al. 2008, *AcA*, 58, 263
- Morton, T. 2014, PhD thesis, California Institute of Technology
- O’Donovan, F. T., Charbonneau, D., Torres, G., et al. 2006, *ApJ*, 644, 1237
- Obermeier, C., Henning, T., Schlieder, J. E., et al. 2016, *AJ*, 152, 223
- Pace, G., Pasquini, L., & François, P. 2008, *A&A*, 489, 403
- Parviainen, H. 2015, *MNRAS*, 450, 3233
- Parviainen, H. 2016, PyDE, v1.5, Zenodo, doi:10.5281/zenodo.45602
- Pepper, J., & Gaudi, B. S. 2005, *ApJ*, 631, 581
- Pepper, J., Stanek, K. Z., Pogge, R. W., et al. 2008, *AJ*, 135, 907
- Petigura, E. A., Howard, A. W., & Marcy, G. W. 2013, *PNAS*, 110, 19273
- Plavchan, P., Latham, D., Gaudi, S., et al. 2015, arXiv:1503.01770
- Pope, B. J. S., Parviainen, H., & Aigrain, S. 2016, *MNRAS*, arXiv:1606.01264
- Press, W. H., Teukolsky, S. A., Vetterling, W. T., & Flannery, B. P. 1992, *Numerical Recipes in FORTRAN. The Art of Scientific Computing*
- Quinn, S. N., White, R. J., Latham, D. W., et al. 2012, *ApJL*, 756, L33
- Quinn, S. N., White, R. J., Latham, D. W., et al. 2014, *ApJ*, 787, 27
- Rojas-Ayala, B., Covey, K. R., Muirhead, P. S., & Lloyd, J. P. 2012, *ApJ*, 748, 93
- Sato, B., Izumiura, H., Toyota, E., et al. 2007, *ApJ*, 661, 527
- Schlegel, D. J., Finkbeiner, D. P., & Davis, M. 1998, *ApJ*, 500, 525
- Schlieder, J. E., Crossfield, I. J. M., Petigura, E. A., et al. 2016, *ApJ*, 818, 87
- Skrutskie, M. F., Cutri, R. M., Stiening, R., et al. 2006, *AJ*, 131, 1163
- Smith, J. C., Stumpe, M. C., Van Cleve, J. E., et al. 2012, *PASP*, 124, 1000

- Stassun, K. G., Collins, K. A., & Gaudi, B. S. 2016, arXiv:1609.04389
- Stassun, K. G., Kratter, K. M., Scholz, A., & Dupuy, T. J. 2012, *ApJ*, 756, 47
- Stumpe, M. C., Smith, J. C., Van Cleve, J. E., et al. 2012, *PASP*, 124, 985
- Twicken, J. D., Chandrasekaran, H., Jenkins, J. M., et al. 2010, *Proc. SPIE*, 7740, 77401U
- Van Cleve, J. E., Howell, S. B., Smith, J. C., et al. 2016, *PASP*, 128, 075002
- van Leeuwen, F. 2009, *A&A*, 497, 209
- van Saders, J. L., & Gaudi, B. S. 2011, *ApJ*, 729, 63
- Vanderburg, A., & Johnson, J. A. 2014, *PASP*, 126, 948
- Vogt, S. S., Allen, S. L., Bigelow, B. C., et al. 1994, *Proc. SPIE*, 2198, 362
- von Braun, K., Lee, B. L., Seager, S., et al. 2005, *PASP*, 117, 141
- Wright, J. T., Marcy, G. W., Howard, A. W., et al. 2012, *ApJ*, 753, 160